Results in Engineering 13 (2022) 100379

Contents lists available at ScienceDirect

Results in Engineering

journal homepage: www.sciencedirect.com/journal/results-in-engineering

Cockle (*Anadara granosa*) shells-based hydroxyapatite and its potential for defluoridation of drinking water

Stanslaus G. Mtavangu [a,b,c,*], Wilson Mahene [b], Revocatus L. Machunda [b], Bart van der Bruggen [a,d], Karoli N. Njau [b]

[a] Department of Chemical Engineering, Faculty of Engineering Sciences, KU Leuven, Celestijnenlaan 200F, B-3001, Leuven, Belgium
[b] Department of Water and Environmental Science and Engineering, Nelson Mandela African Institution of Science and Technology, Arusha, PO Box 447, Tanzania
[c] Department of Chemistry, Dar es Salaam University College of Education, P.O Box 2329, Dar es Salaam, Tanzania
[d] Faculty of Engineering and the Built Environment, Tshwane University of Technology, Private Bag X680, Pretoria, 0001, South Africa

ARTICLE INFO

Keywords:
Cockle (*Anadara granosa*) shells
Hydroxyapatite
Adsorption
Defluoridation
Box-Behnken design

ABSTRACT

The present study describes the synthesis and characterization of a hydroxyapatite (HAp)-based adsorbent derived from biogenic cockle (*Anadara granosa*) shells for the defluoridation of drinking water. The raw cockle shells and synthesized HAp were characterized by X-ray fluorescence spectroscopy (XRF), attenuated total reflection-Fourier transform infrared (ATR-FTIR), X-ray diffraction (XRD), Field emission scanning electron microscopes-energy dispersive X-ray (FESEM-EDX) and Brunauer-Emmett-Teller (BET) surface area analysis. As demonstrated by FTIR, cockle shells were found to be composed of calcium carbonate (97.4%), an aragonite polymorphous type of carbonate mineral. XRD and SEM analysis supported the formation of a nanocrystalline HAp with an average crystal size of 19.08 nm and 57.1 nm, respectively, with a surface area of 105.8 m^2/g and a pore size of 5.6 nm, as depicted by BET. Batch adsorption experiments were conducted using the Box-Behnken design (BBD) with five input parameters: adsorbent dose (2–10 g/L), initial fluoride concentration (10–80 mg/L), contact time (0.5–24 h), reaction temperature (303–333 K), and pH. (3–11). BBD revealed the following optimum conditions: adsorbent dose (6 g/L), initial fluoride concentration (45 mg/L), contact period 12.25 h, reaction temperature (303 K), and pH 3. Experimentally, the adsorption of fluoride on HAp fitted well with the non-linear Langmuir isotherm and linear pseudo-second order kinetics, signifying the chemisorption process. A maximum adsorption capacity (q_m) of 15.374 mg/g, which is closer to the experimental value of 14.053 mg/g, was presented by the Langmuir isotherm. Thermodynamically, the adsorption process was spontaneous, endothermic, and stable in nature. The defluoridation mechanism was through electrostatic attraction, ion exchange, hydrogen bonding, and precipitation. Furthermore, the synthesized HAp and bone char were used to examine their efficacy in defluoridating field water: HAp performed better at natural pH, where the treated water met WHO and TBS standards, whereas bone char had insufficient fluoride removal, especially at high fluoride levels. As a result, this study suggests that HAp derived from *Anadara granosa* shells could be a viable adsorbent for the defluoridation of drinking water.

1. Introduction

Fluoride contamination in groundwater affects the quality of drinking water in different parts of the world [1]. High fluoride concentrations in groundwater are ascribed to geochemical processes and ion exchange within the world's fluoride belts [2–5]. Fluoride is found in fluoride bearing rocks such as cryolite (Na_3AlF_6), fluorite (CaF_2) and fluoroapatite ($Ca_5(PO_4)_3F$) and leaches out to water under favorable conditions. In addition, wastewater discharge from industrial activities that utilize fluorine-containing compounds as raw materials contributes to fluoride recharge to surface water [6]. Fluoride concentrations of 1.5–4.0 mg/L, 4.0–10.0 mg/L, and >10.0 mg/L, respectively, cause dental, skeletal, and crippling fluorosis [7]. As a result, the permissible fluoride levels for bone and dental enamel strengthening should not exceed 1.5 mg/L [8]. However, a concentration below 0.5 mg/L results to dental caries particularly to young children.

* Corresponding author. Department of Chemical Engineering, Faculty of Engineering Sciences, KU Leuven, Celestijnenlaan 200F, B-3001, Leuven, Belgium.
E-mail address: smtavangu@gmail.com (S.G. Mtavangu).

https://doi.org/10.1016/j.rineng.2022.100379
Received 2 January 2022; Received in revised form 25 February 2022; Accepted 27 February 2022
Available online 3 March 2022

About 260 million people in 28 countries rely on groundwater supplies with high fluoride concentrations above the WHO recommendation [9,10], with fourteen in Africa, including Tanzania, eight in Asia, and six in America, primarily tropical [8]. As a result, people in these places are more vulnerable to endemic fluorosis. It is projected that about 80 million people living in East African Rift Valley (EARV) regions unveil a wide range of fluorosis signs due to persistent exposure to fluoride above the allowable limit through drinking water [8,9]. Furthermore, studies have shown that within the EARV, countries like Ethiopia, Kenya, Eritrea and Tanzania are mostly affected by endemic fluorosis [5,6,11,12]. Endemic fluorosis has been recorded in various parts of Tanzania's northern regions, including Arusha, Kilimanjaro, and Manyara, where over 2 million people are at danger of dental, skeletal, and crippling fluorosis [5,13]. Around 80% of the water in these areas comes from groundwater sources; however, the presence of fluoride has rendered many of these sources unsafe for consumption. As a result, community intervention actions are unavoidable.

Several water treatment technologies have been deployed to combat health effects caused by fluoride ingestion. These include ion exchange [14], precipitation [15] electrodialysis [16] nanofiltration [17] and adsorption [6,18]. However, several limitations hinder their application. For instance, chemical dosage by alum may result in the formation of sludge, and Alzheimer disease is possibly related to leached aluminum. Membrane based technologies (dialysis, electrodialysis, reverse osmosis and nanofiltration) are not cost effective in remote areas as they require a constant supply of power and skilled personnel. These limitations have credited adsorption as the viable and feasible technology for defluoridation because of its simplicity and availability of a wide range of adsorbent materials [19].

In Tanzania defluoridation by bone char as adsorbent has been a viable technology for decades, because of its availability and ease in preparation. Bone char emanates from animal bones charred at a temperature range of 500–600 °C; its effectiveness has been concluded in various studies [13,20,21]. It is mainly composed of hydroxyapatite (HAp), a calcium phosphate with exchangeable hydroxide ion. The low stability of hydroxyapatite ($Ca_5(PO_4)_3OH$), with solubility constant Ksp $= 2.34 \times 10^{59}$ allows the exchange of hydroxide ions with fluoride ions from water to form the more stable fluoroapatite ($Ca_5(PO_4)_3F$), Ksp $= 3.16 \times 10^{60}$ [6]. Despite its reported defluoridation effect, the low adsorption capacity, harboring of microbes, cultural and religious inhibitions limit the application of bone char.

Alternatively, synthetic hydroxyapatite ($Ca_{10}(PO_4)_6(OH)_2$) has been prepared by mimicking the HAp structure present in bone chars [22–24]. HAp is a non-toxic calcium phosphate system with high defluoridation capacity [6,24–26]. Many HAp adsorbents have been synthesized and studied, and their effectiveness has been suggested [23,27]. However, the potential application of these materials in the field is not easily achievable, due to the cost associated with their production and therefore, the use of alternative precursors becomes inevitable. Biogenic materials have been reported for their potential sources of cation for HAp synthesis [24,26,28–35]. These can be alternative calcium sources due to their richness in calcium carbonate. Therefore, their availability and abundancy prompted many researchers to study their potential.

Cockle shells (*Anadara granosa*) belonging to the *Arcidae* family are bio-waste of *Mollusca phylum* that is among the sea shells waste that can be found along the shores of oceans and some oceanic food industries [36–38]. In Tanzania tonnes of these shells are found along the shores of the Indian ocean, with no other valuable use apart from being used as home ornaments. Furthermore, their potential for synthesizing HAp for biomedical purposes has been reported by various researchers [36–38]. This is due to richness in calcium carbonate ranging from 89 to 99% [39], that can be used as calcium precursor for HAp synthesis. Studies have reported the defluoridation capacity of HAp derived from different biogenic sources such as crab and prawn shells to be 13.6 and 8.5 mg/g, respectively [24], where else *Limacine artica* shells derived HAp was observed to have a defluoridation capacity of 28.57 mg/g [26]. To the best of our knowledge, no study has considered the synthesis of HAp derived from *Anadara granosa* shells for defluoridation of drinking water. Furthermore, the defluoridation performance of the novel HAp is compared with that of bone char (BC); a current defluoridation technology in northern regions of Tanzania.

Conventional studies of adsorption involve varying one factor while keeping others constant. This does not portray the interactive effect of factors at once and therefore, more time will be used to determine the optimal levels of factors. These limitations can be eliminated by optimizing the effects of variables by a statistical experimental design such as response surface methodology (RSM) that mimics the actual experimental conditions. RSM is a statistical and mathematical tool used for designing experiments, improving, optimizing experimental conditions to reduce trial and error methods and evaluating the significance of process variables even under complex interactions [40,41]. In this study RSM by Box Behnken design (BBD) has been applied to investigate the interactions effects between adsorbent dose, temperature, initial fluoride concentration, pH, and reaction time on defluoridation by hydroxyapatite.

2. Materials and methods

Materials: Cockle (*Anadara granosa*) shells were collected along the shores of the Indian Ocean in Bagamoyo - Coastal region, Kunduchi and Dar es Salaam fish market (popular as "Feri") in Dar es Salaam (Tanzania), where there is an abundance of these shells.

Chemicals: Hydrochloric acid (HCl), sodium hydroxide (NaOH), phosphoric acid (H_3PO_4), ammonium hydroxide (NH_4OH), sodium chloride (NaCl), glacial acetic acid (CH_2COOH), sodium fluoride (NaF) were purchased from Sigma Aldrich, Germany. All the chemicals and reagents used in the experiments were of analytical grade. All the aqueous solutions were prepared by using double distilled water and the pH was adjusted by using 0.1 M of NaOH or HCl.

2.1. Preparation of the cockle shells

The cockle shells were washed thoroughly with tap water using a brush, then rinsed with double distilled water to remove any debris or other impurities. Shells were allowed to dry under sunlight for 12 h, followed by oven drying at 105 °C for 24 h. Then, they were ground into powder by a ball milling machine and were ready for use.

2.2. Synthesis of adsorbent

Hydroxyapatite (HAp) was successfully synthesized from *Anadara granosa* shell powder by a chemical precipitation method adopted from the literature [24]; however, ageing was allowed without stirring. About 100 g of powdered cockle shells were oven dried at 105 °C for 2 h then cooled in a desiccator, followed by digestion (deproteination) with 0.25 M NaOH at room temperature for 2 h, to remove any binding materials. Then the powder (residue) was rinsed with double distilled water to neutral pH and dried in an oven at 105 °C for 1 h. Digested powder shells were demineralized by using 2 M HCl and left for 24 h at room temperature for a total conversion of calcium compounds to calcium chloride as per equation (1) to obtain the filtrate.

$$CaCO_{3(s)} + 2HCl_{(aq)} \rightarrow CaCl_{2(aq)} + CO_{2(g)} + H_2O_{(l)} \quad (1)$$

The filtrate obtained after demineralization was used to determine the concentration of calcium ion (Ca^{2+}) by titration using 0.1 M EDTA and calcon indicator ($C_{21}H_{14}N_2O_7S.2H_2O$), which depicts a color change from pink to blue at the end of the reaction. In a typical procedure, HAp was synthesized by mixing 300 ml of 0.225 M $CaCl_2$ liquor from cockle shells powder acid extract (cation source) and 300 ml of 0.135 M H_3PO_4 (anion source) in a 1000 ml beaker while stirring vigorously to maintain

the Ca/P ratio in the HAp lattice structure at 1.67. During synthesis, 28% of ammonia solution was added to $CaCl_2$ liquor dropwise while stirring strongly in order to adjust the pH to 10.25–10.5, then H_3PO_4 was added drop-wise to the mixture while continuously stirring at room temperature to form a white sticky precipitate at a pH of 10.25–10.5, as per equation (2).

$$10Ca^{2+}{}_{(aq)} + \ 6PO4^{3-}{}_{(aq)} + 2OH^{-}{}_{(aq)} \rightarrow Ca_{10}(PO_4)_6(OH)_{2(S)} \quad (2)$$

The mixture was allowed to age at room temperature for 24 h (without stirring) to allow atoms to occupy their equilibrium lattice positions in the crystal structure. The formed precipitates were filtered and rinsed several times with double distilled water to neutral pH. The obtained white sticky precipitates (HAp) were oven dried at 80 °C for 24 h, then ground into powder and stored in an airtight container ready for characterization and use. Similar procedures were followed in synthesizing HAp by using analytical $CaCl_2$ as a cation source.

2.3. Adsorbent characterization

Synthesized HAp samples and raw cockle shell powder were characterized for functional groups, chemical composition, crystallinity phases, morphology, elemental composition, surface area, pore size, and pore volume. The functional groups were ascertained by attenuated total reflection-Fourier transform infrared (ATR-FTIR) spectroscopy (Bruker Optic GmbH 2011 (alpha model, Laser class 1) in transmittance mode and spectral range of 4000–400 cm^{-1} with a spectral resolution of 2 cm^{-1}, chemical composition by X-ray fluorescence spectroscopy (XRF) (Bruker XRF Spectrometer (Model S8 Tiger). The structural characterization and phase purity of HAp samples were analyzed by a Bruker BV 2D PHASER Best Benchtop (PANalytical BV, Amsterdam, the Netherlands) X-ray diffraction (XRD) analyzer with reflection geometry at 2θ values (10–70°) with a step size of 0.005°, working with a Cu Kα radiation source (λ = 0.15406 nm) at 50 kV and 30 Ma. The morphology and elemental composition were analyzed by Zeiss Ultra Plus 55 field emission scanning electron microscopes (FE-SEM) equipped with energy dispersive X-ray (EDX). Specific surface area and pore volume were determined with a nitrogen absorption apparatus (TriStar II 3020 device) by the Brunauer-Emmett-Teller (BET) method at 77 K from N_2 absorption-adsorption isotherms in the relative pressure range (P/Po) of 0.01–1.0, whereas the pore size distribution was calculated by using the Barrett-Joyner-Halenda (BJH) method. The pH reflecting the point of zero charge (pHpzc) was determined by solid addition [42].

2.4. Batch adsorption experiments

Batch experiments were carried out by using both simulated and field water, collected from different areas in northern regions of Tanzania, (Tables 15 and 16). Physicochemical characteristics such as pH, dissolved oxygen (DO), electric conductivity (EC), total dissolved solids (TDS), and temperature, were determined *in situ* by using a HANNA 9829 multiparameter device. Other parameters were determined as prescribed by standard methods for examination of water and wastewater [43]. Simulated water was prepared by dissolving 2.21 g of NaF in 1 L of double distilled water to make 1000 mg/L fluoride stock solution which was used to make different concentrations of fluoride solutions through dilution. During the experiment, 100 ml of fluoride solution with different pH, initial fluoride concentration, temperature, contact time, and adsorbent dose was placed in a 250 ml Erlenmeyer flask. Mixtures were stirred at 150 rpm during the experimental runs. The obtained solution was then centrifuged and the concentrations of residual fluoride ions were analyzed potentiometrically with an Ion Selective Electrode (ISE) connected to a Mettler Toledo compact pH/ion S220 m and Orion Star A211 m for pH determination. Fluorinated water was mixed with total ionic strength buffer (TISAB II) at a ratio of 1:1 before fluoride measurement. Batch experiments for fluorinated field water samples were run by using the optimized dose from BBD experiments. The amount of fluoride adsorbed at equilibrium (q_e) and removal efficiency were calculated by using equations (3) and (4).

$$q_e = \frac{(C_o - C_e)V}{m} \quad (3)$$

$$\text{R.Efficiency } (\%) = \frac{C_o - C_e}{C_o} X\ 100 \quad (4)$$

where q_e is the amount of fluoride adsorbed at equilibrium (g), C_o - initial fluoride concentration (mg/L), C_e-equilibrium fluoride concentration (mg/L), V - volume of fluoride solution (L), and m - mass of adsorbent (HAp) (g).

2.5. Box-Behnken experimental design

A Box–Behnken experimental design was used in this study to determine the effects of major operating variables on fluoride adsorption, but also to find the best variables interactions that yield maximum fluoride removal. Five independent variables in an experimental design model with three levels codes as shown in Table 1, were used. A total of 46 experiments were executed to examine the effects of five independent variables on the fluoride removal efficiency. Non-linear regression was used to fit the second order polynomial equation (5) to experimental data in order to identify the relevant model terms as described by the following quadratic model;

$$Y = \beta_0 + \sum \beta_i x_i + \sum \beta_{ii} x_{ii}^2 + \sum \beta_{ij} x_i x_j \quad (5)$$

where Y is the predicted response function (removal efficiency), β_o is the intercept/model constant, β_i is slope/the linear effect of input factor X_i, β_{ii} is the quadratic effect of input factor X_i and β_{ij} is the linear-by-linear interactive effect between the input factor X_i and X_j.

3. Results and discussion

3.1. Chemical composition analysis of cockle (Anadara granosa) shells

Table 2 and Fig. 1a, show the chemical composition and functional groups of raw cockle shell powder as determined by XRF and ATR-FTIR. Table 2, shows that calcium oxide is the main component of cockle shells, with trace levels of NiO, ZrO_2, and Fe_2O_3. This provides insights that cockle shells are a good source of calcium that can be used as a precursor during the synthesis of hydroxyapatite. Furthermore, Fig. 1a, shows that cockle shells exhibit peaks at 707, 855, 1079, 1449, 1794 cm^{-1}. These are aragonite peaks, which are the main $CaCO_3$ reservoir in cockle shells [37]. Overall, the cockle shells used in this study consist of about 97.4% $CaCO_3$.This is comparable to the amount reported in the literature [37].

Table 1
Experimental range and levels of process variables.

Factors and levels used in design of experiments (BBD)					
Factors	Unit	Code	Low level (-1)	Medium level 0	High level (+1)
Dose ratio	g/L	A	2	6	10
Initial fluoride Concentration	mg/L	B	10	45	80
Contact time	h	C	0.5	12.25	24
Temperature of reaction	Kelvin	D	303	318	333
pH		E	3	7	11

Table 2
Raw cockle shells powder chemical composition by XRF.

Components	Wt (%)
CaO	55.95
MgO	0.39
Na_2O	0.83
SiO_2	0.65
SO_3	0.22
SrO	0.1
Fe_2O_3	0.04
ZrO_2	0.02
Al_2O_3	0.35
NiO	0.01
LOI	**41.45**

3.2. Characterization of synthesized adsorbent (HAp)

The ATR-FTIR spectra of pure and fluoride loaded HAp are presented in Fig. 1b. The presence of PO_4^{3-} was attested by the bands that occurred at 1024 and 1094 cm^{-1} (asymmetric ν_3 stretching bands), 960 cm^{-1} (the symmetric stretching band ν_1) and the degenerate bending vibration bands at 601 and 562 cm^{-1} [26]. The bands appearing at 3571 cm^{-1} and 630 cm^{-1} correspond to the symmetric stretching and liberational modes of OH^- groups in HAp, respectively. The presence of both PO_4^{3-} and structural OH^- bands confirm the formation of HAp. On the other hand, fluoride loaded HAp shows narrower and sharper peaks, hence relatively more distinct, which indicates increased structural order. The shift of P–O stretching peaks at 960–1030 cm^{-1} where, a band shift observed at 1024 to 1030 cm^{-1} might be attributed to adsorption of fluoride ions onto the HAp surface through electrostatic interaction [26]. The band at 3452 cm^{-1} is assignable to the bending modes of adsorbed water. Peaks observed at 1422 $cm^{-1}$and 872 cm^{-1} confirm presence of CO_3^{2-} ions. The locations of the peaks suggest that the ions reside in the HAp lattice structure replacing PO_4^{-3}, B-type substitution domination [26,44,45]. The slight deviation from the traditionally accepted values for B-type substitution (1465, 1413, and 873 cm^{-1}) may be attributed to the presence of both labile and structural CO_3^{2-} ions, and some A-type substitution. The formation of carbonate ions was ascribed to the absorption of atmospheric carbon dioxide by OH^- ions during the synthesis of HAp in highly alkaline conditions [26].

Fig. 2 shows the XRD patterns of pure and fluoride loaded HAp with diffraction peaks at 2θ values = 25.97°, 29.07°, 32.01°, 32.87, 34.05, 35.48, 39.90°, 46.76°, 49.56°, 53.19°, 64.20° with their crystal plane orientations at (002), (210), (211), (300), (202), (301), (130), (222), (213), (004), (323) respectively. The presence of these peaks confirms the formation of the hexagonal phase of HAp with lattice parameters a = b = 9.4240 and c = 6.8790 as per JCPDS card 01-074-0565. This corresponds to other findings [23,24,26]. There is an observed shift and concurrent decrease in peaks intensity in fluoride loaded HAp from 25.97° to 26.16°, 32.01°–32.28°, 32.87 to 33.05, 39.90°–40.08°, 53.19°–53.32° and 64.20°–64.38°. This suggests the anchoring of fluoride ions on HAp, which was also depicted by FTIR results. The average crystalline size of pure and fluoride loaded HAp were 19.08 and 19.4 nm, respectively, as determined by the Debye Scherrer equation (eq. (6)). The observed increase in particles size may be attributed to fluoride anchoring in the HAp crystal lattice, which induces strong H-bonding with bulk water molecules; this resulted to more agglomeration of HAp particles, and thus an increase in size.

$$D = \frac{K\lambda}{\beta_{2\theta} Cos\theta} \quad (6)$$

where D is the average crystallite size in nm, K = Scherrer constant; equal to 0.9, λ is the specific wavelength of X-ray used (0.154 nm), θ is the diffraction angle and $\beta_{2\theta}$ is the angular width in radians at intensity equal to full width and half maximum (FWHM).

The FESEM images of the pure and fluoride loaded HAp (Fig. 3a) show that most particles are agglomerated and appeared spherical with an average size of 57.2 nm. However, the images of the fluoride loaded HAp showed change in the morphology by increasing in agglomeration as depicted in the particle size analysis from FESEM micrographs where

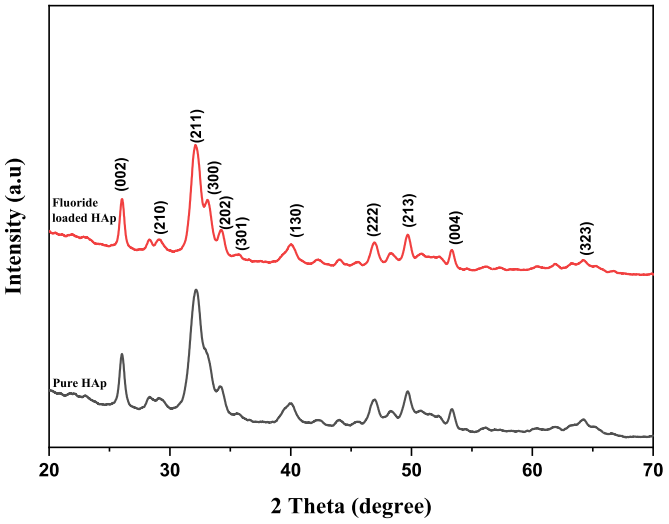

Fig. 2. XRD patterns of pure and fluoride loaded HAp.

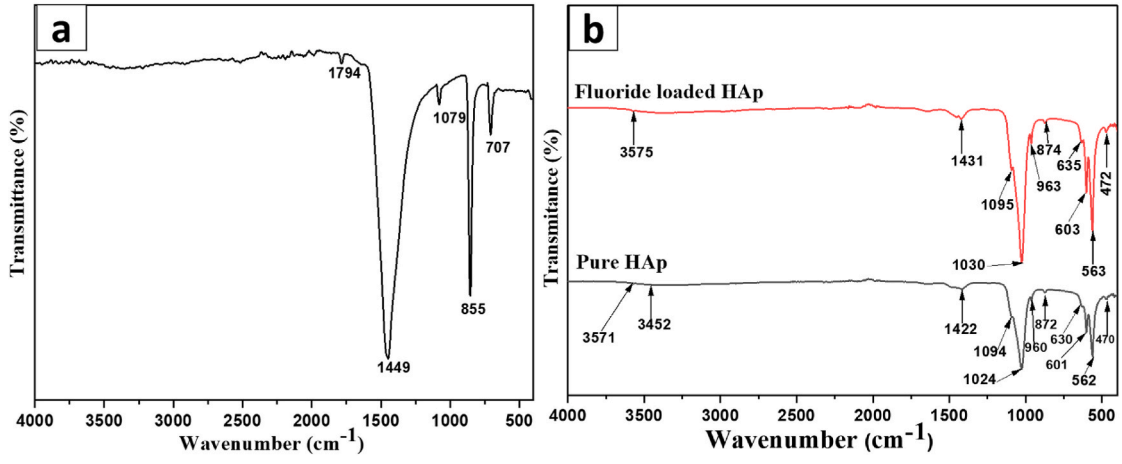

Fig. 1. FTIR spectrum of cockle (*Anadara granosa*) shells powder (a), FTIR spectra of pure and fluoride loaded HAp derived from cockle (*Anadara granosa*) shells (b).

the average size was observed to increase from 57.2 to 81.1 nm. This might be attributed to H-bonding between adsorbed fluoride ions and water molecules, which leads to more agglomeration of HAp particles.

Fig. 3b presents the EDX spectrum of pure HAp with Ca, P and O as the major elements confirming the successful synthesis of HAp. The inset to Fig. 3b shows a description of the percentage weight composition of elements in the HAp. The presence of Si in a trace amount of about 0.19 wt % might be ascribed to the SiO_2 residual observed in *Anadara granosa* shells powder (Table 2) that might have been incorporated in the crystal lattice of HAp during synthesis. The Ca/P molar ratio is an important parameter that ensures chemical homogeneity, solubility and phase purity of HAp [45]. According to EDX analysis, the synthesized HAp has an average Ca/P molar ratio of 2.23. This value shows a positive deviation from the stoichiometric value of 1.67 for stoichiometric HAp, which depict a probable non-stoichiometric HAp of the synthesized sample.

Fig. 4 shows a typical N_2 adsorption–desorption isotherms for HAp and BJH plot (inset) of pore size distribution for unloaded (a) and loaded fluoride (b) HAp. The BET surface area and BJH pore size were 105.8 m^2/g and 5.6 nm for unloaded HAp and 86.9 m^2/g and 5.3 nm for fluoride loaded HAp (Table 3). The observed decrease in surface area of HAp provided insight on the evidence of fluoride anchoring on HAp. This phenomenon may be attributed to the increase in crystalline size as was also depicted by FESEM and XRD analysis. Furthermore, bone char collected from the defluoridation Centre in Arusha Tanzania (for comparison), presented a surface area and pore size of 40.1 m^2/g and 4.1 nm, respectively. This is lower that the surface area presented by synthesized HAp. As a consequence, cockle shells derived HAp could be an effective adsorbent for fluoride removal. According to the porosity classification of the International Union of Pure and Applied Chemistry (IUPAC), material pores are categorized as microporous <2 nm, mesoporous 2–50 nm and macroporous >50 nm. Therefore, synthesized HAp adsorbent is mesoporous in nature [46] with type III isotherm.

3.3. Box –Behnken statistical analysis

The suitability of a model to represent fluoride removal by HAp was tested by sequential model sum of squares and model summary statistics, and results are presented by fit summary in Table 6. The quadratic model was found to have maximum adjusted R-squared and predicted R-squared values with a p value of <0.01 and was chosen for further analysis. Practical relationship conveyed by a second-order polynomial equation with interaction terms was fitted between the experimental results obtained on the basis of BBD and the input variables. The final equation obtained in terms of actual variables is:

$$R.Efficiency\ (\%)\ 71.1998 + 18.7445\ \text{x A} - 20.5014\ \text{x B} + 10.77\ \text{x C} + 6.80056\ \text{x D} - 18.4166\ x\ E + 4.97875\ x\ AB - 0.872425\ x\ AE + 5.86625\ x\ BC + 15.6167\ x\ DE - 6.8237\ x\ A^2 - 2.66312\ x\ E^2 \quad (7)$$

ANOVA was used to check the significance and fitness of the model by various assigned criteria. Table 4, shows that the model has an F-value of 92.2, p value < 0.05, indicating that it is significant. Furthermore, a model is valid if the lack of fit is not significant (p value > 0.05). Results show a p value of 0.1854, this implies a favorite model. Predicted R^2 is used to measure how well the model predicts a response value, and for the desired model, the difference between adjusted R^2 and predicted R^2 should be approximately 0.20. The results from this study show the predicted R^2 of 0.9323 is in reasonable agreement with the adjusted R^2 of 0.9581(Table 5). Moreover, adequate precision measures the range between the predicted response and its associated error. It provides insight in the signal-to-noise ratio; therefore, its desired value should be 4 or above. Our results show a ratio of 38.7354, implying an adequate signal. The p value was used to determine the significance of the regression coefficient value as shown in equation (5), to indicates the interaction between variables. Table 4 shows that the interactions of AB, BC, DE, A^2, and E^2 were significant with p values < 0.05, but the AE interaction was not (p > 0.05). Results were also checked for normality of residuals. A normality plot shown in Fig. 7i, shows that the data points on these plots lie reasonably close to a straight line. Furthermore, the relationship between the actual and predicted values of removal efficiency is shown in Fig. 7j. It is obvious that the developed model is adequate since the data points lie close to the diagonal line.

3.4. Effects of variable interaction on the fluoride removal efficiency

On the basis of the quadratic model, three-dimensional response surface plots and their corresponding contours were plotted for studying the effects variables interactions on fluoride removal efficiency.

3.4.1. Interaction effects of adsorbent dose and initial fluoride concentration

The interaction effects of adsorbent dose and initial fluoride concentration on fluoride removal efficiency are shown in Fig. 5a, b at 12.25 h, 318 K, pH 7. There is an observed increase in fluoride removal efficiency from 71.19 to 98.64% as the adsorbent dose increased from 3 to 10 g/L with concurrent increase in initial fluoride concentration up to about 45 mg/L. This is attributed to large surface areas and the availability of more adsorptive sites for fluoride attachment at higher adsorbent dosages. However, at a fluoride initial concentration of above 45 mg/L, the removal efficiency is observed to decrease from 71.19 to 20.15%. This is attributed to the occupancy of available active sites on the adsorbent at a high initial fluoride concentration. A similar trend was also reported elsewhere [47].

3.4.2. Interaction effects of pH of solution and adsorbent dose

Fig. 5 (c, d) show how the combined effects of pH and adsorbent dose impact on fluoride removal at an initial fluoride concentration of 45 mg/L, time of 12.25 h, temperature of 318 K. It was observed that fluoride removal efficiency increased from 71.19 to 99.75% at a pH below 7.2 (pHpzc). Further pH increases above 7.2 resulted in a decrease in removal efficiency from 71.19 to 25.42% at a pH of 11. This is attributed to a change in the surface charge of the adsorbent that can be described by the point of zero charge (pHpzc) of HAp, which was found to be 7.2

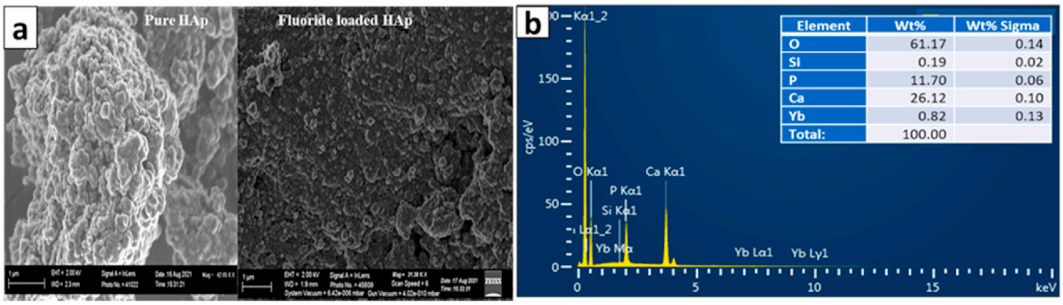

Fig. 3. FESEM image of pure and fluoride loaded HAp (a) EDX spectrum of synthesized HAp (b).

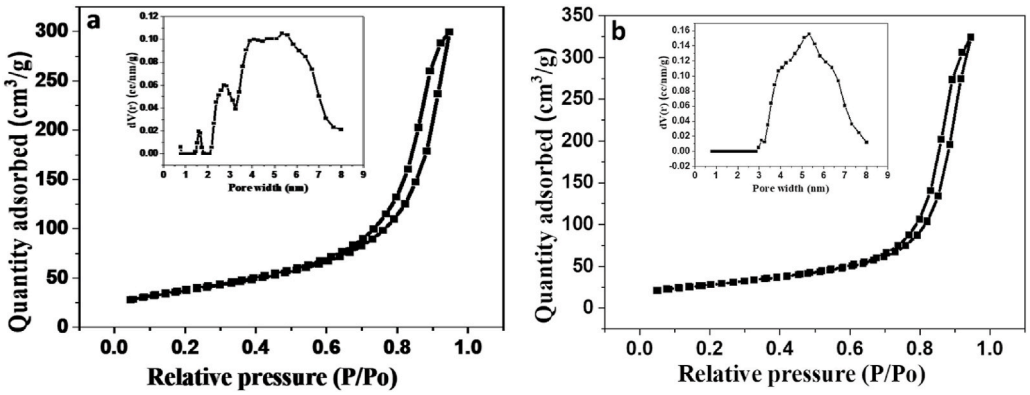

Fig. 4. N_2 adsorption–desorption isotherms for HAp and (inset) BJH plot of pore size distribution of unloaded fluoride (a) and loaded (b) HAp.

Table 3
Surface area, pores size, pore volume of adsorbents.

Adsorbent	Surface area S_{BET} (m^2/g)	Pore size (nm)	Pore volume V_{BJH} (cm^3/g)
HAp before fluoride loading	105.8	5.6	0.43
HAp after fluoride loading	86.9	5.3	0.45
Bone char	40.1	4.1	0.15

(Fig. 8). When the pH of the solution is below the pHpzc, the surface of HAp becomes more positively charged due to protonation effect of the hydroxyl (OH^-) group. This phenomenon favors the electrostatic attraction of adsorbate (fluoride ions) on the adsorbent surface. There is a decrease in removal efficiency at pH above the pHpzc, which can be attributed to the negatively charged surface of HAp due to the deprotonation effect of hydroxyl groups. This results in repulsion between the fluoride ions and the HAp surface, thus decreasing the removal efficiency. Similar results were also reported in the literature [26,42]. The observed increase in fluoride removal was also combined by the adsorbent dose, where a higher removal was observed at 10 g/L. This is attributed to the presence of a large number of adsorptive sites on the HAp surface at higher dosages.

3.4.3. *Interaction effects of initial fluoride concentration and contact time*

Fig. 6 (e, f) presents the interaction effects between initial fluoride concentration and contact time on the defluoridation efficiency at a dose of 6 g/L, temperature 318 K, pH 7. Fluoride adsorption onto HAp was investigated at different initial fluoride concentrations that ranged from 10 to 80 mg/L. At low initial fluoride concentrations, the results show an increase in fluoride removal efficiency with increasing time. Removal efficiencies from 79.9% to 96.60% were observed when the initial fluoride concentration was decreasing from 45 to 10 mg/L, while the contact time was increasing from 0.5 to 24 h as portrayed by a contour plot (Fig. 6 f). The reason for this trend can be attributed to the

Table 5
Model statistics for model validation.

Statistical parameters	Values of developed Model
R^2	0.9674
Adjusted R^2	0.9581
Predicted R^2	0.9323
Adeq. Precision	38.7354
Std. Dev.	4.61
Mean	67.9
C.V. %	6.79

Table 6
Fit summary of the model.

Source	Sequential p-value	Lack of Fit p-value	Adjusted R^2	Predicted R^2	
Linear	<0.0001	0.0222	0.8788	0.8533	
2FI	0.0034	0.0614	0.926	0.8708	
Quadratic	**0.0029**	**0.1618**	**0.9551**	**0.9062**	**Suggested**
Cubic	0.5427	0.1008	0.954	0.4904	Aliased

Table 4
ANOVA for response surface reduced quadratic model.

ANOVA for reduced quadratic model						
Source	Sum of Squares	df	Mean Square	F-value	p-value	
Model	22087.54	11	2007.96	92.2	<0.0001	significant
A-Dose ratio	5621.67	1	5621.67	258.14	<0.0001	
B-Initial fluoride concentration	6724.9	1	6724.9	308.8	<0.0001	
C-Contact time	1855.89	1	1855.89	85.22	<0.0001	
D-Temperature of reaction	739.96	1	739.96	33.98	<0.0001	
E-pH	5426.74	1	5426.74	249.19	<0.0001	
AB	99.15	1	99.15	4.55	0.0402	
AE	3.04	1	3.04	0.1398	0.7108	
BC	137.65	1	137.65	6.32	0.0168	
DE	975.53	1	975.53	44.79	<0.0001	
A^2	474.94	1	474.94	21.81	<0.0001	
E^2	72.34	1	72.34	3.32	0.0772	
Residual	740.45	34	21.78			
Lack of Fit	**687.89**	**29**	**23.72**	**2.26**	**0.1854**	**not significant**
Pure Error	52.55	5	10.51			
Cor Total	22827.99	45				

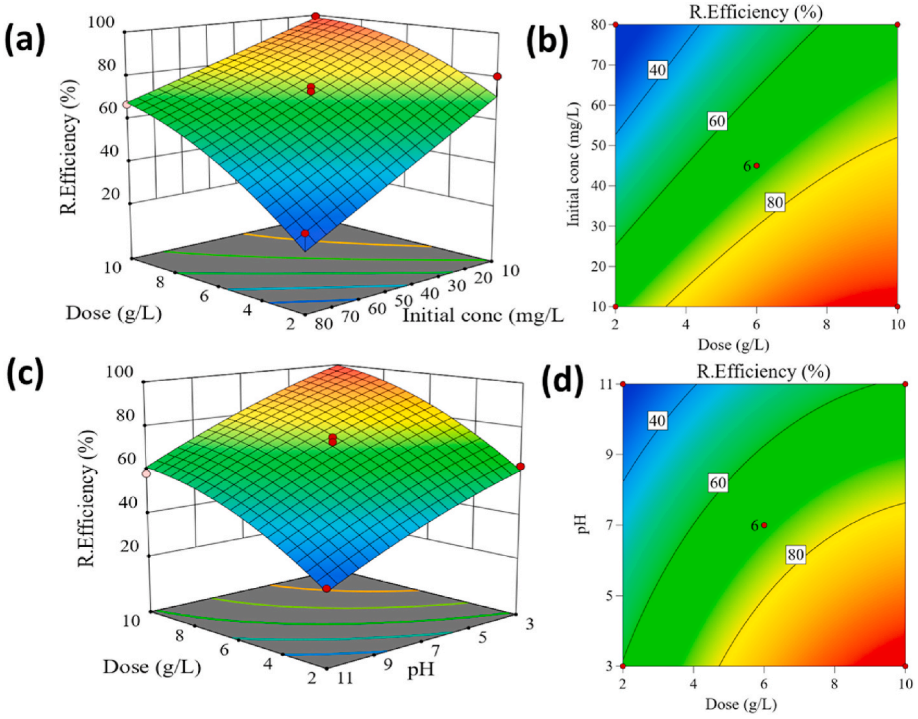

Fig. 5. Response surface -3D and contour plots showing the interactions effect of (a, b) adsorbent dose and initial fluoride concentration, at time 12.25 h, temperature 318 K, pH 7, (c, d) pH and adsorbent dose at initial fluoride concentration of 45 mg/L, time 12.25 h, temperature 318 K on fluoride removal efficiency.

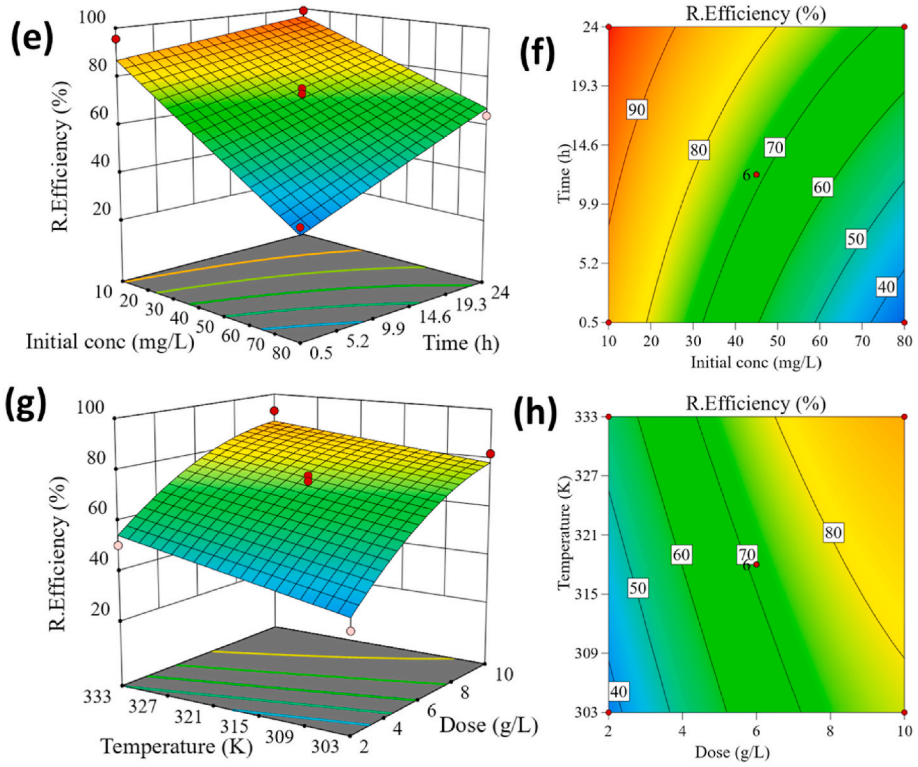

Fig. 6. Response surface -3D and contour plots showing the interactions effect of (e, f) initial fluoride concentration and contact time at adsorbent dose of 6 g/L, temperature 318 K, pH 7, (g, h) temperature and adsorbent dose at initial fluoride concentration of 45 mg/L, time 12.25 h and pH 7, on fluoride removal efficiency.

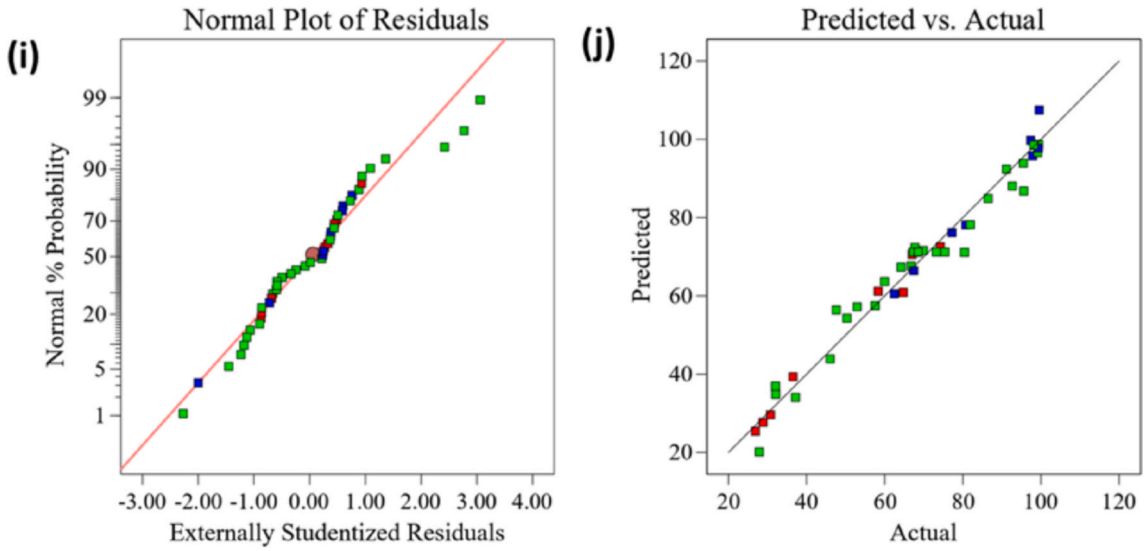

Fig. 7. Normal probability plot and residual error for fluoride removal efficiency by HAp (i) predicted vs experimental values of fluoride removal efficiency (j).

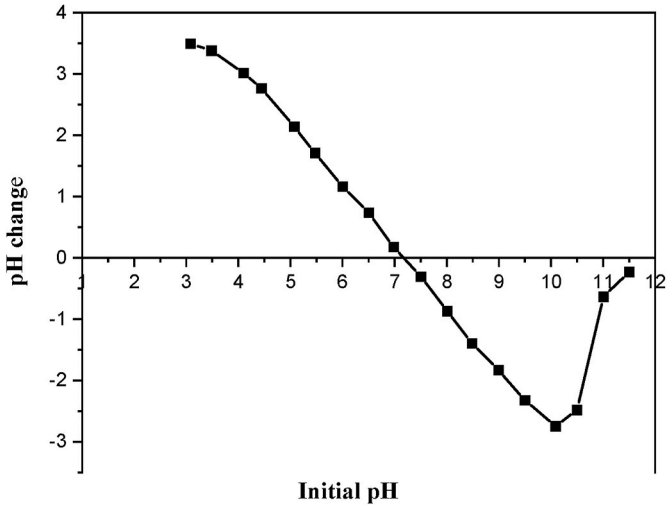

Fig. 8. pHpzc of HAp derived from cockle (Anadara granosa) shells.

availability of adsorptive sites at an adsorbent dose of 6 g/L and increase in adsorbate-adsorbent interaction time. However, the occupancy of adsorptive sites was limited to an initial fluoride concentration of greater than 45 mg/L due to adsorbent saturation, which resulted in a decrease in fluoride removal efficiency, which was also reported elsewhere [26,48].

3.4.4. *Interaction effects of temperature of reaction and adsorbent dose*

The interaction effects of temperature and adsorbent dose on fluoride removal efficiency at an initial fluoride concentration of 45 mg/L, time 12.25 h and pH 7, was executed at a temperature range of 303–333 K and a dose of 2–10 g/L, Fig. 6g, h. It was observed that fluoride removal efficiency increased simultaneously with increase in adsorbent dose and reaction temperature. An increase in the fluoride removal with the adsorbent dosage can be attributed to a larger surface area of adsorbent and the availability of more adsorption sites. Furthermore, fluoride removal was observed to increase with temperature, which provides an insight that the defluoridation by HAp is favorably adsorbed at higher temperatures, which implies that the adsorption process may be an endothermic [26]. A maximum fluoride removal of 88.0% was observed at a dose of 10 g/L and a temperature of 333 K. Similar findings were also reported by Ref. [42].

3.5. *Optimization by using desirability functions*

The optimized conditions for maximum removal of fluoride by HAp depicted by the model are adsorbent dose of 6 g/L, an initial fluoride concentration of 45 mg/L, contact time of 12.25 h, temperature 303 K, pH 3 with a desirability of one. Triplicate confirmatory experiments were run and results are presented in Table 7, where the efficiency of fluoride removal was found to be 94.5, 94.7, 94.9% and a defluoridation capacity of 7.08, 7.10, 7.12 mg/g for experiments 1, 2 and 3, respectively, while the model prediction was 95.8% and 7.68 mg/g for removal efficiency and defluoridation capacity, respectively. This shows a good agreement between the experimental and predicted values.

3.6. *Adsorption isotherms*

Langmuir and Freundlich isotherms are the most used models in articulating the relationship between the adsorbate and adsorbent at the solid-solution interface due to their good description of experimental data in a large range of operating conditions. Linearized and non-linearized models of both Langmuir and Freundlich have been studied; results show that non-linear models present better fit to experimental data with minimal statistical error [49,50]. The Langmuir isotherm describes the adsorption process on a monolayer and a homogeneous surface of an adsorbent with equal adsorptive sites that do not allow an alliance of adsorbate molecules in adjacent monolayer sites. It is a chemical adsorption process (chemisorption). The non-linearized and linearized forms of the Langmuir isotherm are represented by equations (8) and (9) respectively.

$$q_e = \frac{q_m b C_e}{1 + b C_e} \tag{8}$$

$$\frac{C_e}{q_e} = \frac{1}{q_m b} + \frac{C_e}{q_m} \tag{9}$$

where q_e - amount of adsorbate per unit mass of adsorbent (mg/g), C_e - equilibrium concentration of the adsorbate (mg/L), q_m - amount of adsorbate at complete monolayer coverage (mg/g), b - Langmuir isotherm constant (L/mg) indicating the rate of sorption. Its linear and non-linear plots can be expressed as C_e/q_e vs C_e and qe vs Ce respectively. The affinity between fluoride ions and HAp can be predicted using the Langmuir parameter b from the dimensionless separation

Table 7
Numerical optimization confirmatory experimental results.

	Dose	Initial fluoride conc	Final fluoride conc	pH	Time	Experimental RE	Predicted RE	Experimental DC	Predicted DC
Run	g/L	mg/L	mg/L		h	%	%	mg/g	mg/g
1	6	45	2.47	3	12.25	94.51	95.77	7.08	7.68
2	6	45	2.38	3	12.25	94.72	95.77	7.10	7.68
3	6	45	2.28	3	12.25	94.94	95.77	7.12	7.68

factor R_L as per equation (10).

$$R_L = \frac{1}{1 + bC_o} \tag{10}$$

where C_o - initial fluoride concentration and b - Langmuir isotherm constant. The value of R_L indicating if the adsorption is favorable ($0 < R_L < 1$), unfavorable ($R_L > 1$), linear ($R_L = 1$), irreversible ($R_L = 0$).

The Freundlich isotherm model describes the physical adsorption processes on a heterogeneous system and multilayer surfaces. It, therefore, presumes a heterogeneous surface of the adsorbent with unequal adsorption sites having different adsorption energies [51,52]. The Freundlich isotherm model is represented by non-linear equation (11) and linear equation (12). The linear and non-linear Freundlich isotherm plots can be expressed as Log q_e vs Log C_e and qe vs Ce, respectively.

$$q_e = K_F C_e^{1/n} \tag{11}$$

$$\mathrm{Log}q_e = \mathrm{Log}K_F + \frac{1}{n}\mathrm{Log}C_e \tag{12}$$

where, q_e - amount of adsorbate adsorbed at equilibrium per unit weight of adsorbent (mg/g), C_e - equilibrium concentration of the adsorbate (mg/L), K_F - adsorption capacity, and n - adsorption intensity, where if $n > 1$ imply favorable adsorption, $n = 1$ linear adsorption, $n < 1$ unfavorable adsorption.

Table 8 shows the adsorption parameters of the linear Langmuir and linear Freundlich isotherm models, where the R^2 value for the linear Freundlich isotherm model is higher than that of the linear Langmuir isotherm model, confirming the better fitting of experimental data by the linear Freundlich isotherm model. The feasibility of adsorption by both models was tested by calculating the R_L and n values at different temperatures. Results from Table 8 show that the R_L values were found to fall between 0 and 1 and $n > 0$; which indicates that the conditions were favorable for adsorption in both linear Langmuir and linear Freundlich isotherms. Similar results were also reported by Refs. [52,53].

Fig. 9 (a, b, c) shows the experimental data plots of non-linear Langmuir and non-linear Freundlich isotherm models at 303, 318, and 333 K. Their isotherm parameters are listed in Table 9 where the non-linear Langmuir isotherm model presented higher correlation coefficient (R^2) values and lower chi-square (X^2) values compared to the non-linear Freundlich isotherm model. This provides insights that the non-linear Langmuir isotherm model shows a better fit to the adsorption experimental data. Furthermore, the non-linear Freundlich isotherm model had n values less than zero ($n < 0$) at all temperatures. This confirms that the non-linear Freundlich model had a poor fit to the experimental data. A statistical error analysis was executed to compare the linear and non-linear isotherm models' fitness to experimental data by observing the X^2 and R^2 values. The non-linear Langmuir isotherm model presented the highest R^2 values [54] compared to other linear and non-linear isotherm models studied in this work. This fact was further supported by low chi-square (X^2) values of the non-Langmuir isotherm as shown in Table 9. Therefore, by using R^2 values, the order of model fitness to the experimental data is non-linear Langmuir isotherm > linear Freundlich isotherm > non-linear Freundlich isotherm > linear Langmuir isotherm. Therefore, this signifies that the adsorption of fluoride ions on HAp was well presented by the non-linear Langmuir isotherm model, which confirms the chemisorption process that normally occurs at wide temperature range [49]. On the other hand, the non-Langmuir adsorption capacity (q_m) values were observed to increase with a rise in temperature (Table 9). This is attributed to the high demand for energy that facilitates the breaking of bonds of the reactants to allow more kinetic and collision of reacting molecules that influence adsorption. This implies that the bond formation between adsorbent and adsorbate is chemical and, thus, the chemisorption process was favored endothermically [53]. Furthermore, the high q_m values reported at all temperatures can also be geared by the nature of the adsorbent (HAp) with monolayer coverage and a structured homogenous surface with a finite number of identical sites as was supported by XRD studies (Fig. 2) where only hydroxyapatite phases (a defluoridation agent) are present in the adsorbent [24]. The non-linear Langmuir isotherm presented a maximum adsorption capacity (q_m) of 15.374 mg/g, which is close to the experimental value of 14.053 mg/g. This confirms the suitability of the model to the experimental data. Similar results are also reported in the literature [55]. A comparison of the maximum adsorption capacities for fluoride removal over various adsorbents is given in Table 10.

Table 8
Linear isotherm model parameters for adsorption of fluoride onto HAp.

Adsorption isotherm models	Parameters	Temperature (K)		
		303	318	333
Langmuir	q_{max} (mg/g)	12.204	13.554	15.198
	b (L/mg)	0.016	0.017	0.018
	R_L	0.866	0.857	0.848
	R^2	0.856	0.859	0.861
Freundlich	K_F ($mg^{1-1/n}L^{1/n}g^{-1}$)	0.325	0.389	0.469
	n	1.397	1.413	1.428
	R^2	0.975	0.974	0.972

3.7. Adsorption kinetic modeling

The kinetics of fluoride adsorption on synthesized HAp was examined by applying pseudo-first order and second order kinetic model represented by non-linear form equations (13) and (14) respectively. In pseudo first order, the rate of reaction is proportional to the concentration of the reactants. Nonetheless, pseudo second order is based on the assumption that the rate of occupation of adsorption sites is limited to the number of unoccupied sites and considers chemisorption as the rate limiting step. Furthermore, due to limitations of the aforementioned models to describe the diffusion mechanism of solute into the interior of adsorbent intraparticle diffusion model was included in this study. Plots for non-linear pseudo first order and non-linear pseudo second order can be derived from q_t as y-axis and t as x-axis.

$$q_t = q_e(1 - e^{-(K_1 t)}) \tag{13}$$

$$q_t = \frac{q_e^2 K_2 t}{1 + q_e K_2 t} \tag{14}$$

where, q_t represents the amount of fluoride ions adsorbed by HAp at time t (mg/g), q_e represents the amount of fluoride ions adsorbed at equilibrium (mg/g), K_1 represents the pseudo-first-order rate constant (min^{-1}), and K_2 represents the pseudo-second-order rate constant (g/mg min). The suitability of the two models was established by constructing a linear plot of ln (qe - qt) vs. t, for the pseudo first order and t/qt vs. t for

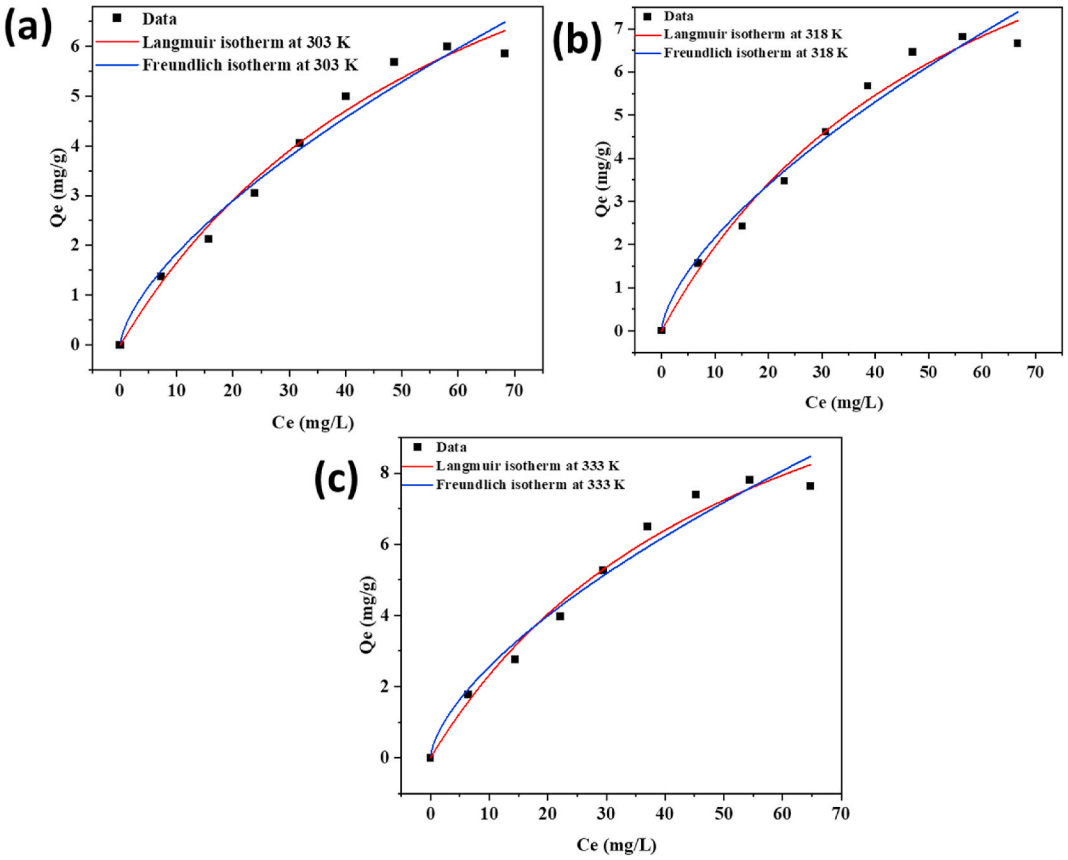

Fig. 9. Non-linear plots for Langmuir and Freundlich isotherms at (a) 303 K, (b)318 K and (c) 333 K.

Table 9
Non-linear isotherm model parameters for adsorption of fluoride onto HAp.

Adsorption isotherm models	Parameters	Temperature (K)		
		303	318	333
Langmuir	q_{max} (mg/g)	12.228	13.645	15.374
	b (L/mg)	0.016	0.017	0.018
	R_L	0.865	0.857	0.849
	R^2	0.9801	0.9795	0.9789
	X^2	0.0933	0.1246	0.1686
Freundlich	K_F ($mg^{1-1/n}L^{1/n}g^{-1}$)	0.406	0.487	0.585
	n	0.656	0.648	0.641
	R^2	0.9462	0.9443	0.9425
	X^2	0.1717	0.2302	0.3122

the pseudo second order model represented by their linear expression equations (15) and (16), respectively.

$$In(q_e - q_t) = Inq_e - K_1 t \quad (15)$$

$$\frac{t}{q_t} = \frac{1}{K_2 q_e^{\,2}} + \frac{t}{q_e} \quad (16)$$

Fig. 10 (a, b) shows the linear pseudo-first order and linear pseudo-second order kinetic plots of the fluoride adsorption on the HAp at different temperatures. The estimation of parameters from both kinetic orders of adsorption and their correlation coefficient R^2 are presented in Table 11. According to error analysis, linear pseudo-second order kinetics has higher R^2 values than linear pseudo-first order kinetics (Table 11). This shows a better fit of the experimental data by a linear pseudo-second-order kinetic model. It can be seen that the fluoride adsorption capacity at equilibrium (q_e) by HAp increases with an increase in temperature [60]. This might be attributed to an increase in the kinetic and collision of adsorbate and adsorbent ions as temperature increases.

Fig. 10 (c, d) shows the non-linear pseudo first order and non-linear pseudo second order kinetic plots of the fluoride adsorption on the HAp at different temperatures of 303, 318, and 333 K. Results from Table 12 show that all the R^2 values in the non-linear pseudo second order model

Table 10
Summary of adsorption capacity of various adsorbents used for defluoridation process.

Adsorbent	Fluoride concentration range (mg/L)	Dose (g/L)	pH	Maximum adsorption capacity (q_{max}) (mg/g)	Reference
Nano-hydroxyapatite/stilbite	2–200	10	–	9.15	[6]
Hydroxyapatite nanowire	1–200	0.5	7	40.65	[56]
Octacalcium phosphate	40–140	4	8	26.8	[57]
Hydroxyapatite-crabs derived	5–70	5	3	13.6	[24]
Hydroxyapatite-prawns derived	5–70	5	3	8.5	[24]
Nano-sized HAp	9.5–133	2	6.5	11	[58]
Bone char	5–80	2	7	5.92	[59]
Brushite	20–50	8	6	6.59	[19]
Phospogysum HAp	10–50	10	7	40.818	[27]
HAp *Anadara granosa* derived	10–80	6	3	15.374	This study

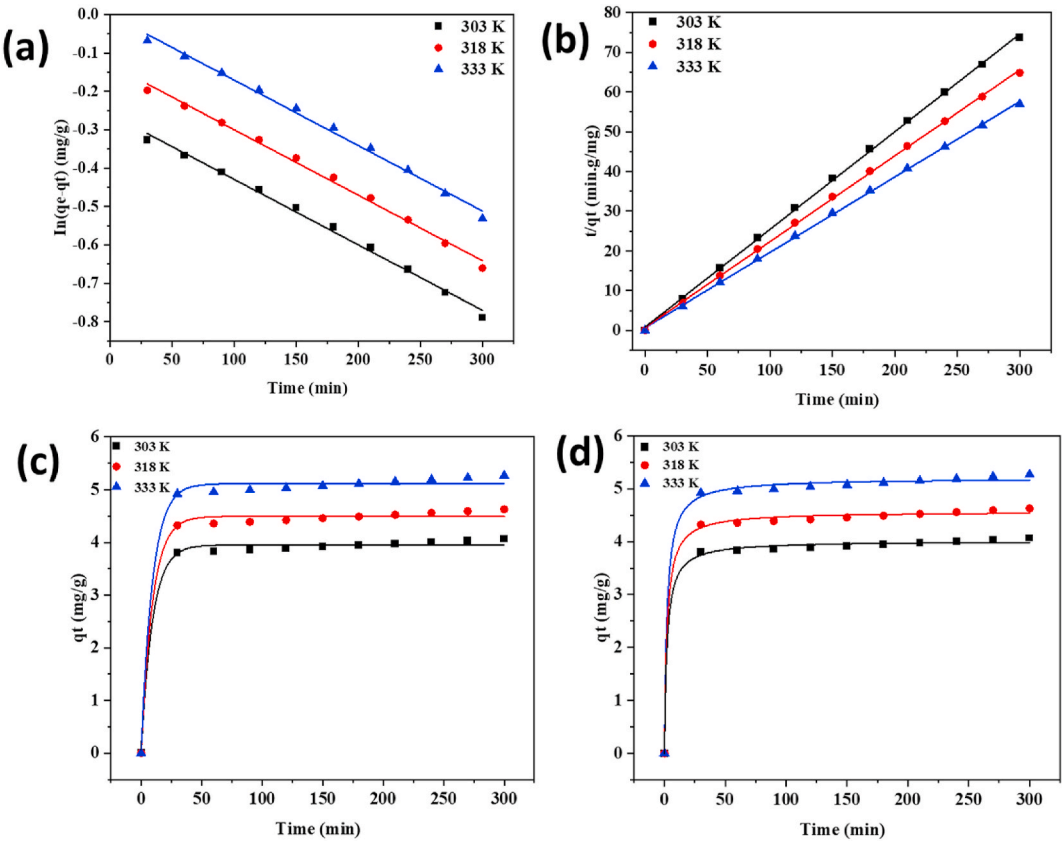

Fig. 10. Kinetic adsorption isotherms for (a) linear pseudo first order (PFO), (b) linear pseudo second order (PSO), (c) non-linear pseudo first order (PFO) and (d) non-linear pseudo second order (PSO).

Table 11
Linear kinetic model parameters for adsorption of fluoride onto HAp.

Adsorption kinetic models	Parameters	Temperature (K)		
		303	318	333
Pseudo first order (PFO)	q_e (mg/g)	0.666	0.816	0.999
	K_1 (min^{-1})	0.002	0.001	0.002
	R^2	0.9938	0.9938	0.9938
Pseudo second order (PSO)	q_e (mg/g)	4.067	4.628	5.267
	K_2 (g/mg min)	0.07	0.061	0.054
	R^2	0.9995	0.9995	0.9995

have higher values than the non-linear pseudo first order at all temperatures. On the other hand, the fitness of experimental data to the kinetic model is accepted when the X^2 value is small. From Table 12, the X^2 values presented by the non-linear pseudo second order kinetic model are smaller than those of the non-linear pseudo first order model at all temperatures. This reveals that the non-linear pseudo-second order kinetic model better fits the experimental data. The suitability of linear and non-linear kinetic models in fitting the experimental data can be compared by observing the values obtained from the error analysis method. However, the accuracy of the linear and non-linear models depends on the type of adsorbate, adsorbent, and conditions of the experimental. Tables 11 and 12 show the values for correlation coefficient (R^2) and chi-square (X^2) that were used to evaluate the fitness of the linear and non-linear kinetic models. Based on the R^2 and X^2 error functions the non-linear pseudo-second order kinetic model fit the experimental data better [50,61]. However, by observing the R^2 values, the established model fitness trend is linear PSO > non-linear PSO > no-linear PFO > linear PFO. This provides insight that a linear pseudo-second order kinetic model presents a better fit of experimental data [50]. Furthermore, a pseudo-second order model is used to describe chemical processes such as electron exchange and ion exchange between adsorbates and adsorbents [50]. This suggests that the chemisorption process was dominated during the adsorption of fluoride onto HAp.

Table 12
Non-linear kinetic model parameters for adsorption of fluoride onto HAp.

Adsorption kinetic models	Parameters	Temperature (K)		
		303	318	333
Pseudo first order (PFO)	q_e (mg/g)	3.9476	4.4923	5.1121
	K_1 (min^{-1})	0.1072	0.1072	0.1072
	R^2	0.9959	0.9959	0.9959
	X^2	0.0058	0.0075	0.0097
Pseudo second order (PSO)	qe (mg/g)	4.0122	4.5658	5.1958
	K_2 (g/mg min)	0.1161	0.1020	0.0896
	R^2	0.9981	0.9981	0.9981
	X^2	0.0028	0.0036	0.0046

3.7.1. *Intraparticle diffusion model (IPD)*

Apart from the rate laws, the intraparticle diffusion model was used to investigate the rate limiting step of the adsorption of fluoride onto HAp by using equation (17), which is plotted by qt vs $t^{1/2}$ where q_t is the amount of solute on the surface of the sorbent at time t (mg/g), K_p is the intra-particle rate constant (mg/g $min^{1/2}$), t is the time (min), and C (mg/g) is a constant showing the thickness of the boundary layer. Fig. 11 shows a plot of qt vs $t^{1/2}$ at different temperatures, in which three adsorption steps are presented. The first step is represented by a steeper region. This is regarded as adsorption by bulk diffusion of fluoride that occurred on the external surface of the adsorbent. It is attained rapidly and depends on the surface area of the adsorbent (HAp). The second step is represented by a gradual region; this reflects the gradual adsorption stage, which shows that intraparticle diffusion is the rate-limiting step. Step 3 is the equilibrium stage, during which intraparticle diffusion

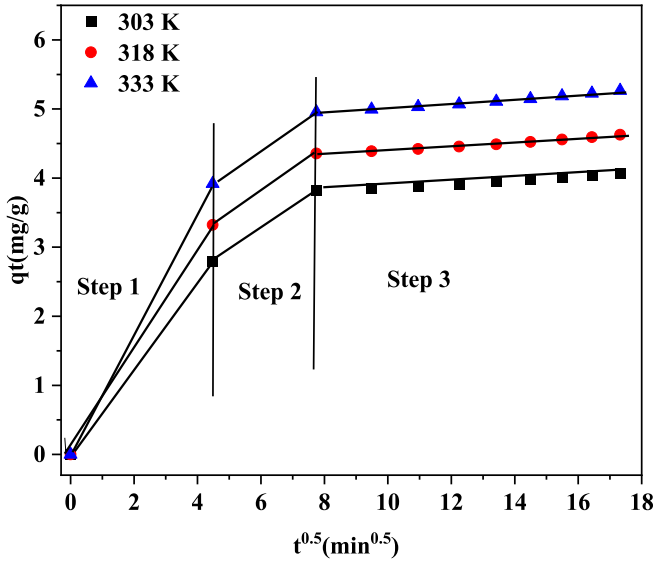

Fig. 11. Weber-Morris intraparticle diffusion model for adsorption of fluoride onto HAp at different temperatures.

slows due to the extremely low adsorbate concentration in the solution [62]. This indicates that the transport of adsorbate ions from solution to the active surface of the adsorbent and pores may be responsible for ions uptake. Furthermore, results from Table 13 show that the K_p value increased with a rise in temperature, which signifies an increase in the rate of adsorption. The C value indicates the boundary layer thickness, in which an increase in C value results in an increase in the boundary layer effect. Results from Table 13 show an increase in C values with temperature. This reflects the high rate of diffusion of ions in the boundary layer, which was also depicted by the Kp values. Therefore, since the C value is not zero for all temperatures, this shows that intra-particle diffusion may not be the controlling factor in determining the kinetics of the process [27,61]. Conclusively, the pseudo-second-order kinetic model suggested a better fit for the adsorption of fluoride on the HAp than the pseudo-first-order model and intra-particle diffusion model.

$$q_t = K_p t^{1/2} + C \quad (17)$$

3.8. Thermodynamic properties of adsorbent

Thermodynamic parameters of the adsorption process, such as standard free energy change (ΔG^o), standard enthalpy change (ΔH^o) and standard entropy change (ΔS^o) were calculated using the following change in Gibbs free energy:

$$\Delta G^\circ = -RT \ln k_d \quad (18)$$

According to the Gibbs free energy

$$\Delta G^\circ = \Delta H^\circ - T\Delta S^\circ \quad (19)$$

where ΔG^o is the standard free energy change (kJ mol^{-1}), ΔH^o is the standard enthalpy change (kJ mol^{-1}) and ΔS^o is the standard entropy change (kJ mol^{-1} K^{-1}). T is the temperature (K), R is the universal gas constant (8.314 $Jmol^{-1}$ K^{-1}) and K_d is the adsorption equilibrium constant. The equations (18) and (19) can be merged to form equation (20).

$$\ln K_d = \frac{\Delta S^o}{R} - \frac{\Delta H}{RT} \quad (20)$$

The value of sorption equilibrium constant K_d was determined according to method suggested by Ref. [63]. Furthermore, the standard enthalpy change (ΔH^o) and the standard entropy change (ΔS^o) were calculated from the slope and intercept of a Van't Hoff plot ($\ln K_d$ versus 1/T) (eq. (20)) as shown in Fig. 12. The positive values of ΔG^o, ΔH^o and ΔS^o indicate that the sorption process is spontaneous, endothermic, and stable, respectively. However, if the reaction is non-spontaneous, exothermic, and unstable, these thermodynamic properties show negative values. Results from Table 14 show the negative value of ΔG^o and the positive value of ΔH^o, confirming that the fluoride removal by HAp was governed by spontaneous and endothermic reactions [22,26], whereas the positive value of ΔS^o provides insight on the stability and affinity of HAp for fluoride ions [64]. This implies that the adsorption of fluoride onto HAp under this study was governed by chemisorption process which can work over a wide range of temperature than physisorption [49].

Table 13
Parameters of the intraparticle diffusion (IPD) model.

Kinetic diffusion model	Parameter	Temperature (K)		
		303	318	333
Intraparticle diffusion model	K_p (mg/g $min^{1/2}$)	0.023	0.026	0.03
	C (mg/g)	3.649	4.153	4.726
	R^2	0.9727	0.9727	0.9727

3.9. Effect of competing anions on fluoride removal efficiency by HAp

The fluoride removal efficiency of HAp was evaluated in the presence of co-ions commonly available in water that include nitrate (NO_3^-), sulphate (SO_4^{2-}), chloride (Cl^-), carbonate (CO_3^{2-}) and bicarbonate (HCO_3^-). The experimental conditions were fixed at an initial fluoride concentration of 10 mg/L, adsorbent dose of 6 g/L, reaction temperature of 303 K, pH 7 and a fixed concentration of 100 mg/L for each co-ion. The results from Fig. 13 show a significant decrease in fluoride removal efficiency in the presence of carbonate, followed by bicarbonate and sulphate. When compared to other anions, NO_3^- and Cl^- have the least negative effects on fluoride removal efficiency. Presence of carbonate and bicarbonate decreased the removal efficiency significantly due to an increase in solution pH attributed by OH^- ions from CO_3^{2-} and HCO_3^- hydrolysis, as shown in equations (21) and (22), respectively [65]. Due to the comparable ionic radius of the fluoride ion (1.36 Å) and the hydroxyl ion (1.40 Å), the increased OH^- ions concentration compete with fluoride on the active site, which lowers fluoride removal [66]. However, CO_3^{2-} caused a very low removal efficiency compared to HCO_3^- due to its high dissociation constant (K_b) value, which enabled the high release of OH^- ions [67]. A similar trend was also reported

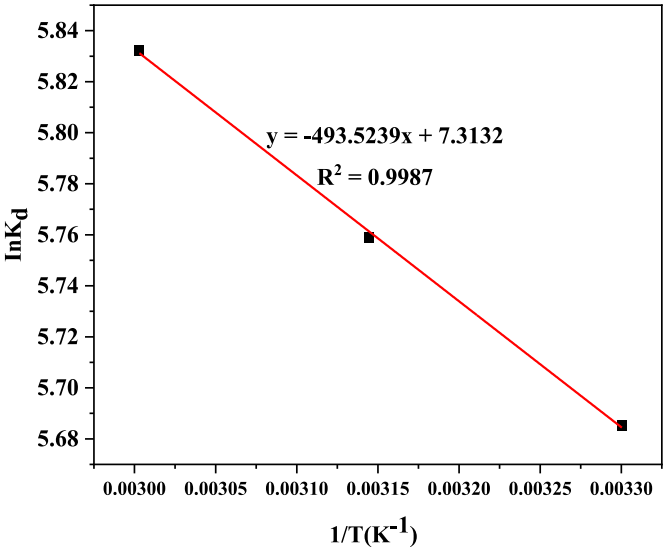

Fig. 12. Van't Hoff plot for fluoride adsorption onto HAp.

Table 14
Thermodynamic parameters for the adsorption of fluoride ions by HAp.

Temperature (K)	ΔG° KJ/mol	ΔH° (KJmol^{-1})	ΔS° (KJk^{-1}mol^{-1})
303	−14.322	4.103	0.061
318	−15.226		
333	−16.147		

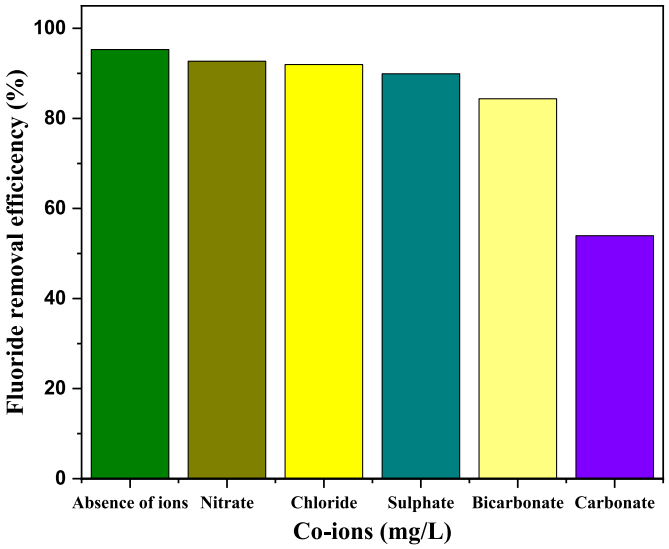

Fig. 13. Influence of co-ions on fluoride removal efficiency by HAp.

elsewhere [68].

$$CO_{3^{2-}(aq)} + H_2O_{(1)} \rightleftharpoons HCO_{3^-(aq)} + OH^-_{(aq)}, K_b = 2.0 \times 10^{-4} \quad (21)$$

$$HCO_{3^-(aq)} + H_2O_{(1)} \rightleftharpoons H_2CO_{3(aq)} + OH^-_{(aq)}\ K_b = 2.5 \times 10^{-8} \quad (22)$$

3.10. Defluoridation of field water samples

Synthesized HAp was used to investigate its effectiveness in fluoride removal from field water with the physicochemical characteristics shown in Table 15. Aside from cockle shell-derived HAp (BV), synthetic HAp derived from analytical reagents (STD) and bone char (BC) compared under similar adsorption conditions (adsorbent dose of 6 g/L, temperature 303 K, time 12 h). Results from Table 16 show that (BV) had high removal efficiencies compared to (STD) and (BC). The reason for its outstanding performance may be credited to the presence of other cations [24] as per XRF results (Table 2), in which on their dissolution in water, their metal ions might have contributed to complexing the fluoride ions. Poor performance of bone char could be attributed to its small surface area, which could have been attributed to a few adsorptive sites (Table 3). Similar results were also reported in the literature [6,24].

3.11. Defluoridation mechanism

Various studies have elucidated the mechanisms of fluoride adsorption, which include electrostatic attraction, ion/ligand exchange, H-bonding, and precipitation [27,69,70]. Under this study, fluoride adsorption mechanisms by HAp were investigated through FTIR, XRD, FESEM, and BET studies, Figs. 1b, 2 and 3a, and 4 respectively. In Fig. 1b the shift or disappearance of bands related to OH^- and PO_4^{3-}groups after adsorption was attributed to fluoride-exchange with OH-groups in the HAp lattice due to their ionic size [61] (ligand exchange) and the formation of fluorapatite, as shown by equation (23). A similar scenario was presented from FTIR studies [70]. Furthermore, the increase in crystal size after adsorption depicted from XRD and FESEM studies, was assumed to be caused by fluoride anchoring on HAp by electrostatic attraction, particularly at low pH. This might have attributed to induced H-bonding, which lead to agglomeration of HAp particles (eq. (24)). This phenomenon was more evinced by BET analysis (Fig. 4) where a decrease in surface areas of HAp after adsorption was observed due to the increase in crystal size caused by the aforementioned reason.

$$Ca_{10}(PO_4)_6(OH)_2 + nF^- \rightarrow Ca_{10}(PO_4)_6(F)_2 + 2OH^- \quad (23)$$

$$Ca_{10}(PO_4)_6(OH)_2 + nF^- \xrightarrow[\text{Medium}]{\text{Acidic}} Ca_{10}(PO_4)_6(OH^+)_2 - - - nF^- \quad (24)$$

Moreover, the precipitation mechanism can be ascribed to fluoride removal in this study. Researchers have observed the formation of soluble $Ca(OH)_2$ and insoluble dicalcium phosphate (eq. (25)) at pH levels lower than 4.8 [26,71]. As a result, the presence of soluble $Ca(OH)_2$ could have attributed to fluoride removal via precipitation reaction (eq. (26)) [26].This was also verified in this study, in which, through a hydroxyapatite leaching test, a concentration of calcium ions of 24.08, 2.28 and 0.01 mg/L was determined titrimetrically in fluoride solution of 10 mg/L and a dose of 6 g/L at a pH of 3, 7, 11 respectively. High concentration of calcium ions at low pH compared to high pH, might have attributed to more precipitation of fluoride ions, hence high removal efficiency, which was observed to be 98.76, 87.98, and 26.45% at pH of 3, 7, and 11, respectively. Concurrently, spectrophotometrically the amount of leached phosphate (PO_4^{-3}) from HAp at pH of 3, 7, and 11 was determine and found to be 8.9, 2.5, and 17.4 mg/L respectively.

$$Ca_{10}(PO_4)_6(OH)_2 \rightarrow 6CaHPO_4.2H_2O + 4Ca(OH)_2 \quad (25)$$

$$Ca(OH)_{2(aq)} + F^-_{(aq)} \rightarrow CaF_{2(s)} + OH^-_{(aq)} \quad (26)$$

Therefore, driving forces for adsorption of fluoride ions on HAp in this study could be depicted by electrostatic forces, H-bonding, ligand exchange and precipitation reaction (Fig. 14).

3.12. Regeneration and reusability of adsorbent (HAp)

The recovery of the adsorbents is an important part of the practical applications of the adsorbents. In order to verify the feasibility of reuse of the HAp, a 0.1 M NaOH solution was used as an eluent. The adsorbent

Table 15
Physico-chemical characteristics of field water.

Sample ID	DO	Temp	EC	TDS	NO_3^-	PO_4^{3-}	Total Hardness	Cl^-
	mg/L	°C	μS/cm	mg/L	mg/L	mg/L	mg/L	mg/L
S1	5.39	23.65	992	496	13	0.74	8	52.5
S2	6.15	22.88	415	208	16.8	0.66	5.15	24.6
S3	6.29	21.25	329	164	16.4	0.48	7.55	17.5
S4	6.77	20.1	488	243	22.2	0.44	6.8	22.14
S5	6.71	22.5	1918	960	7	0.73	8.1	93.6
S6	7.91	26.2	806	395	20	1.41	10	56
S7	8.31	26.1	1219	605	6	1.03	12.8	68.6
S8	6.2	27.1	460	222	26.7	0.54	10	11.67
S9	5.3	26.4	1924	962	46	1.3	18	70
S10	6.4	27.3	1461	730	30	1.6	24	61

Table 16
Batch defluoridation experiments for field water by different adsorbents.

Sample ID	Parameters							
	Initial fluoride (mg/L)	Initial pH	Final fluoride and (final pH) by different adsorbents			Removal efficiency – Y (%)		
			STD	BV	BC	STD	BV	BC
S1	29.05	8.44	2.64 (8.77)	1.15 (8.84)	19.05 (9.00)	90.91	96.04	34.42
S2	9.3	8.46	0.57 (8.44)	0.32 (8.50)	5.40 (8.71)	93.8	96.51	41.91
S3	4.83	7.79	0.08 (8.29)	0.07 (8.22)	1.99 (8.59)	98.36	98.55	58.8
S4	5.03	8.31	0.23 (8.55)	0.19 (8.38)	3.55 (8.76)	95.36	96.19	29.37
S5	31.79	8.73	4.79 (8.89)	1.12 (8.96)	19.97 (9.06)	84.91	96.47	37.17
S6	9.12	7.45	0.46 (8.62)	0.36 (8.72)	4.64 (8.85)	94.91	95.95	49.04
S7	21.35	8.48	1.68 (8.85)	0.93 (8.87)	10.25 (9.04)	92.13	95.63	51.99
S8	6.26	7.42	0.19 (8.49)	0.16 (8.54)	2.86 (8.78)	96.9	97.4	54.31
S9	24.8	7.76	3.80 (8.95)	1.08 (8.97)	15.17 (9.04)	84.66	95.65	38.81
S10	18.9	7.6	1.81 (8.88)	1.07 (8.84)	11.85 (9.01)	90.4	94.33	37.3

STD -synthetic hydroxyapatite, BV- biogenic *Anadara granosa* shells derived hydroxyapatite, BC- bone char.

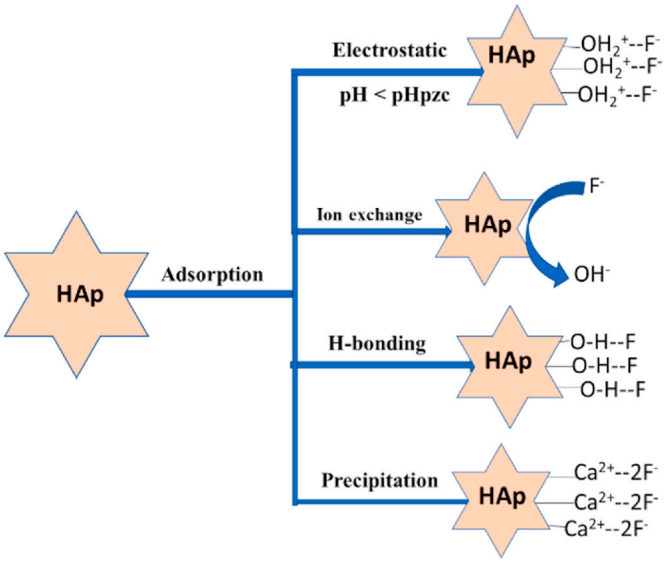

Fig. 14. Defluoridation mechanism of HAp derived from cockle (Anadara granosa) shells.

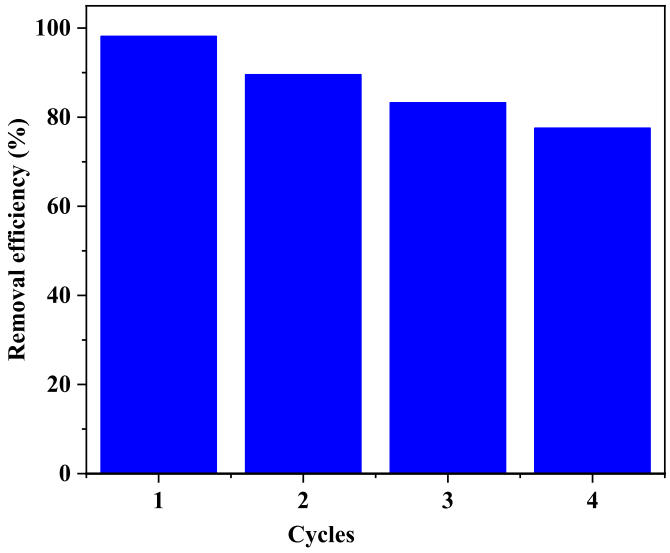

Fig. 15. Regeneration and reusability of HAp using a fluoride solution of 10 mg/L, a dose of 6 g/L, a pH of 7, and a temperature of 303 K.

dose of 6 g/L was soaked in a 10 mg/L fluoride solution for about 12 h. The fluoride-loaded adsorbent was centrifuged, and the supernatant was taken for fluoride analysis. The remaining adsorbent was washed three times with distilled water before being soaked in 0.1 M NaOH for 3 h and then dried in an oven at 80 °C for 6 h. After each cycle, the adsorbent was separated, washed with distilled water, soaked in 0.1 M NaOH, and dried in an oven, ready for the next run. After four run cycles, a slight decrease in the fluoride removal efficiency by HAp was observed, from 98.2 to 77.6% (Fig. 15). This might be attributed to a decrease in HAp purity due to the replacement of hydroxyl groups by fluoride ions.

4. Conclusion

The synthesis of HAp derived from cockle (Anadara granosa) shells as a novel adsorbent for defluoridation was successful in this study. HAp characterization by FTIR, XRD, FESEM, and BET revealed the anchoring of fluoride ions on the adsorbent surface. Fluoride adsorption on the HAp was depicted by narrower, sharper, and distinct peaks, which indicates increased structural order. XRD peak shift confirmed more fluoride loading on HAp. BET studies revealed a decrease in surface area for HAp from 105.8 to 86.9 m^2/g due to an increase in crystal size caused by fluoride anchoring on the adsorbent, which promoted agglomeration. The increase in crystal size was further confirmed by XRD and FESEM studies. Fluoride adsorption mechanisms were observed to be attributed to electrostatic attraction, ion exchange, H-bonding, and precipitation, which were confirmed by FTIR, XRD, FESEM, and BET analysis. Isotherm and kinetic modelling were best described by the non-linear Langmuir model and linear pseudo-second order kinetic model. A theoretical maximum adsorption capacity of 15.374 mg/g for HAp, closer to the experimental value of 14.053 mg/g, was depicted. According to thermodynamic studies, fluoride adsorption on HAp is spontaneous, stable, and performs well at high temperatures. Moreover, unlike bone char, HAp was able to treat a wide range of fluoride concentrations at natural pH levels above the pzc to fluoride levels acceptable by WHO and TBS regulations for drinking water (1.5 mg/L). As a result, the new HAp produced from *Anadara granosa* shells is a promising adsorbent for drinking water defluoridation.

Credit author statement

Stanslaus George Mtavangu: Conceptualization, Methodology, Formal analysis, Investigation, Writing – original draft, Visualization; Wilson Mahene: Methodology, Investigation.; Revocatus Lazaro Machunda: Conceptualization, Methodology, Writing – review & editing, Supervision, Project administration, Funding acquisition.; Bart van der Bruggen: Conceptualization, Methodology, Writing – review & editing, Validation, Supervision, Funding acquisition.; Karoli Nicholas Njau: Conceptualization, Methodology, Writing – review & editing, Supervision, Project administration, Funding acquisition.

Declaration of competing interest

The authors declare that they have no known competing financial interests or personal relationships that could have appeared to influence the work reported in this paper.

Acknowledgments

This work was funded by the Flemish Inter-university Council for University Development Cooperation (VLIR-UOS) under grant number TZ2019IUC029A101 through an Institutional University Cooperation (IUC) programme with the Nelson Mandela African Institution of Science and Technology (NM-AIST).

References

[1] J.P. Maity, et al., Seven 21st Century Challenges of Arsenic-Fluoride Contamination and Remediation, Elsevier, 2021.
[2] M. Vithanage, P. Bhattacharya, Fluoride in drinking water: health effects and remediation, in: CO2 Sequestration, Biofuels and Depollution, Springer, 2015, pp. 105–151.
[3] L.A. Olaka, et al., Groundwater fluoride enrichment in an active rift setting: Central Kenya Rift case study, Sci. Total Environ. 545 (2016) 641–653.
[4] A. Rashid, et al., Fluoride prevalence in groundwater around a fluorite mining area in the flood plain of the River Swat, Pakistan, Sci. Total Environ. 635 (2018) 203–215.
[5] J. Ijumulana, et al., Spatial analysis and GIS mapping of regional hotspots and potential health risk of fluoride concentrations in groundwater of northern Tanzania, Sci. Total Environ. 735 (2020) 139584.
[6] T. Sani, et al., Defluoridation performance of nano-hydroxyapatite/stilbite composite compared with bone char, Separ. Purif. Technol. 157 (2016) 241–248.
[7] A. Bretzler, C.A. Johnson, The geogenic contamination handbook: addressing arsenic and fluoride in drinking water, Appl. Geochem. 63 (2015) 642–646.
[8] WHO, Guidelines for drinking-water quality, WHO Chron. 38 (4) (2011) 104–108.
[9] J. Shen, A.I. Schäfer, Factors affecting fluoride and natural organic matter (NOM) removal from natural waters in Tanzania by nanofiltration/reverse osmosis, Sci. Total Environ. 527 (2015) 520–529.
[10] V. Kimambo, et al., Fluoride occurrence in groundwater systems at global scale and status of defluoridation–state of the art, Groundwater Sustain Develop. 9 (2019) 100223.
[11] B. Thole, *Ground Water Contamination with Fluoride and Potential Fluoride Removal Technologies for East And Southern Africa.* Perspectives in Water Pollution, 2013, pp. 65–95.
[12] E. Vuhahula, et al., Dental fluorosis in Tanzania great Rift Valley in relation to fluoride levels in water and in 'Magadi'(Trona), Desalination 248 (1–3) (2009) 610–615.
[13] H. Mjengera, G. Mkongo, Appropriate deflouridation technology for use in flourotic areas in Tanzania, Phys. Chem. Earth, Parts A/B/C 28 (20–27) (2003) 1097–1104.
[14] C.S. Sundaram, S. Meenakshi, Fluoride sorption using organic–inorganic hybrid type ion exchangers, J. Colloid Interface Sci. 333 (1) (2009) 58–62.
[15] C.F.Z. Lacson, M.-C. Lu, Y.-H. Huang, Fluoride-rich wastewater treatment by ballast-assisted precipitation with the selection of precipitants and discarded or recovered materials as ballast, J. Environ. Chem. Eng. 9 (4) (2021) 105713.
[16] A. Bhatnagar, E. Kumar, M. Sillanpää, Fluoride removal from water by adsorption—a review, Chem. Eng. J. 171 (3) (2011) 811–840.
[17] M. Tahaikt, et al., Fluoride removal from groundwater by nanofiltration, Desalination 212 (1–3) (2007) 46–53.
[18] T. Zhu, et al., Enhanced adsorption of fluoride by cerium immobilized cross-linked chitosan composite, J. Fluor. Chem. 194 (2017) 80–88.
[19] M. Mourabet, et al., Defluoridation of water using Brushite: equilibrium, kinetic and thermodynamic studies, Desalination 278 (1–3) (2011) 1–9.
[20] M. Gourouza, I. Natatou, A. Boos, Elimination of fluoride ions from an aqueous solution with charred beef shoulder blade bones, J. Mater. Environ. Sci. 5 (2) (2014) 416–425.
[21] C. Rojas-Mayorga, et al., Optimization of pyrolysis conditions and adsorption properties of bone char for fluoride removal from water, J. Anal. Appl. Pyrol. 104 (2013) 10–18.
[22] G.E.J. Poinern, et al., Defluoridation behavior of nanostructured hydroxyapatite synthesized through an ultrasonic and microwave combined technique, J. Hazard Mater. 185 (1) (2011) 29–37.
[23] D. Mehta, et al., Synthesis of hydroxyapatite nanorods for application in water defluoridation and optimization of process variables: advantage of ultrasonication with precipitation method over conventional method, Ultrason. Sonochem. 37 (2017) 56–70.
[24] A.W. Wagutu, R. Machunda, Y.A.C. Jande, Crustacean derived calcium phosphate systems: application in defluoridation of drinking water in East African rift valley, J. Hazard Mater. 347 (2018) 95–105.
[25] Y. Wang, et al., Enhanced adsorption of fluoride from aqueous solution onto nanosized hydroxyapatite by low-molecular-weight organic acids, Desalination 276 (1–3) (2011) 161–168.
[26] A. Samant, B. Nayak, P.K. Misra, Kinetics and mechanistic interpretation of fluoride removal by nanocrystalline hydroxyapatite derived from Limacine artica shells, J. Environ. Chem. Eng. 5 (6) (2017) 5429–5438.
[27] D. Zhang, et al., Utilization of waste phosphogypsum to prepare hydroxyapatite nanoparticles and its application towards removal of fluoride from aqueous solution, J. Hazard Mater. 241 (2012) 418–426.
[28] G.S. Kumar, A. Thamizhavel, E. Girija, Microwave conversion of eggshells into flower-like hydroxyapatite nanostructure for biomedical applications, Mater. Lett. 76 (2012) 198–200.
[29] P. Kamalanathan, et al., Synthesis and sintering of hydroxyapatite derived from eggshells as a calcium precursor, Ceram. Int. 40 (10) (2014) 16349–16359.
[30] S. Rujitanapanich, P. Kumpapan, P. Wanjanoi, Synthesis of hydroxyapatite from oyster shell via precipitation, Energy Proc. 56 (2014) 112–117.
[31] A. Shavandi, et al., Synthesis of nano-hydroxyapatite (nHA) from waste mussel shells using a rapid microwave method, Mater. Chem. Phys. 149 (2015) 607–616.
[32] J. Chen, et al., Synthesis of hydroxyapatite nanorods from abalone shells via hydrothermal solid-state conversion, Mater. Des. 87 (2015) 445–449.
[33] A. Pal, et al., Strontium doped hydroxyapatite from Mercenaria clam shells: synthesis, mechanical and bioactivity study, J. Mech. Behav. Biomed. Mater. 90 (2019) 328–336.
[34] M. Umesh, et al., Eggshells Biowaste for Hydroxyapatite Green Synthesis Using Extract Piper Betel Leaf-Evaluation of Antibacterial and Antibiofilm Activity, Environmental Research, 2021, p. 111493.
[35] S.H. Saharudin, et al., Effect of aging time in the synthesis of biogenic hydroxyapatite derived from cockle shell, Mater. Today Proc. 19 (2019) 1208–1215.
[36] A. Danmaigoro, et al., Development of cockleshell (Anadara granosa) derived CaCO3 nanoparticle for doxorubicin delivery, J. Comput. Theor. Nanosci. 14 (10) (2017) 5074–5086.
[37] S.K. Mahmood, et al., Preparation and characterization of cockle shell aragonite nanocomposite porous 3D scaffolds for bone repair, Biochem. Biophys. Rep. 10 (2017) 237–251.
[38] K. Dhanaraj, G. Suresh, Conversion of waste sea shell (Anadara granosa) into valuable nanohydroxyapatite (nHAp) for biomedical applications, Vacuum 152 (2018) 222–230.
[39] O. Jatto, I. Asia, W. Medjor, Proximate and mineral composition of different species of snail shell, Pacific J. Sci. Technol. 11 (1) (2010) 416–419.
[40] M. Mourabet, et al., Use of response surface methodology for optimization of fluoride adsorption in an aqueous solution by Brushite, Arab. J. Chem. 10 (2017) S3292–S3302.
[41] M. Kumari, S.K. Gupta, Response surface methodological (RSM) approach for optimizing the removal of trihalomethanes (THMs) and its precursor's by surfactant modified magnetic nanoadsorbents (sMNP)-An endeavor to diminish probable cancer risk, Sci. Rep. 9 (1) (2019) 1–11.
[42] M. Mourabet, et al., Removal of fluoride from aqueous solution by adsorption on Apatitic tricalcium phosphate using Box–Behnken design and desirability function, Appl. Surf. Sci. 258 (10) (2012) 4402–4410.
[43] APHA, Standard Methods for the Examination of Water and Wastewater, vol. 2, American Public Health Association, 2012.
[44] G.E. Poinern, et al., Synthesis and characterisation of nanohydroxyapatite using an ultrasound assisted method, Ultrason. Sonochem. 16 (4) (2009) 469–474.
[45] N.K. Nga, N.T.T. Chau, P.H. Viet, Facile synthesis of hydroxyapatite nanoparticles mimicking biological apatite from eggshells for bone-tissue engineering, Colloids Surf. B Biointerfaces 172 (2018) 769–778.
[46] J. Kamieniak, et al., Mechanical, pH and thermal stability of mesoporous hydroxyapatite, J. Inorg. Organomet. Polym. Mater. 28 (1) (2018) 84–91.
[47] Y.S. Solanki, et al., Application of synthesized Fe/Al/Ca based adsorbent for defluoridation of drinking Water and its significant parameters optimization using response surface methodology, J. Environ. Chem. Eng. 7 (6) (2019) 103465.
[48] M. Mourabet, et al., Removal of fluoride from aqueous solution by adsorption on hydroxyapatite (HAp) using response surface methodology, J. Saudi Chem. Soc. 19 (6) (2015) 603–615.
[49] J. López-Luna, et al., Linear and nonlinear kinetic and isotherm adsorption models for arsenic removal by manganese ferrite nanoparticles, SN Appl. Sci. 1 (8) (2019) 1–19.
[50] A.R.P. Hidayat, et al., Linear and nonlinear isotherm, kinetic and thermodynamic behavior of methyl orange adsorption using modulated Al2O3@ UiO-66 via acetic acid, J. Environ. Chem. Eng. 9 (6) (2021) 106675.
[51] A.K. Yadav, et al., Defluoridation of groundwater using brick powder as an adsorbent, J. Hazard Mater. 128 (2–3) (2006) 289–293.
[52] N. De Almeida Ohana, L.F. Hm, N.-G. Luis, Adsorption of arsenic anions in water using modified lignocellulosic adsorbents, Results Eng. 13 (2022) 100340.
[53] S. Meenakshi, C.S. Sundaram, R. Sukumar, Enhanced fluoride sorption by mechanochemically activated kaolinites, J. Hazard Mater. 153 (1–2) (2008) 164–172.
[54] R. Han, et al., Study of equilibrium, kinetic and thermodynamic parameters about methylene blue adsorption onto natural zeolite, Chem. Eng. J. 145 (3) (2009) 496–504.
[55] S. Alemu, et al., Water defluoridation by aluminium oxide–manganese oxide composite material, Environ. Technol. 35 (15) (2014) 1893–1903.
[56] J. He, et al., Performance of novel hydroxyapatite nanowires in treatment of fluoride contaminated water, J. Hazard Mater. 303 (2016) 119–130.
[57] A. Idini, et al., Defluoridation of water through the transformation of octacalcium phosphate into fluorapatite, Heliyon 5 (8) (2019), e02288.

[58] V. Sternitzke, et al., Uptake of fluoride from aqueous solution on nano-sized hydroxyapatite: examination of a fluoridated surface layer, Environ. Sci. Technol. 46 (2) (2012) 802–809.
[59] C.K. Rojas-Mayorga, et al., A new synthesis route for bone chars using CO2 atmosphere and their application as fluoride adsorbents, Microporous Mesoporous Mater. 209 (2015) 38–44.
[60] Y.-S. Kim, J.-H. Kim, Isotherm, kinetic and thermodynamic studies on the adsorption of paclitaxel onto Sylopute, J. Chem. Therm. 130 (2019) 104–113.
[61] M.A.E. de Franco, et al., Removal of amoxicillin from water by adsorption onto activated carbon in batch process and fixed bed column: kinetics, isotherms, experimental design and breakthrough curves modelling, J. Clean. Prod. 161 (2017) 947–956.
[62] K.-Y.A. Lin, Y.-T. Liu, S.-Y. Chen, Adsorption of fluoride to UiO-66-NH2 in water: stability, kinetic, isotherm and thermodynamic studies, J. Colloid Interface Sci. 461 (2016) 79–87.
[63] P.S. Ghosal, A.K. Gupta, Determination of thermodynamic parameters from Langmuir isotherm constant-revisited, J. Mol. Liq. 225 (2017) 137–146.
[64] S. Tangsir, et al., Water defluoridation using Al2O3 nanoparticles synthesized by flame spray pyrolysis (FSP) method, Chem. Eng. J. 288 (2016) 198–206.
[65] A.J. Kitalika, et al., Fluoride variations in rivers on the slopes of mount meru in Tanzania, J. Chem. 2018 (2018).
[66] R. Chandrajith, S. Diyabalanage, C. Dissanayake, Geogenic fluoride and arsenic in groundwater of Sri Lanka and its implications to community health, Groundwater Sustain Develop. 10 (2020) 100359.
[67] U. Kumari, S.K. Behera, B. Meikap, A novel acid modified alumina adsorbent with enhanced defluoridation property: kinetics, isotherm study and applicability on industrial wastewater, J. Hazard Mater. 365 (2019) 868–882.
[68] W. Ayinde, et al., Green synthesis of AgMgOnHaP nanoparticles supported on chitosan matrix: defluoridation and antibacterial effects in groundwater, J. Environ. Chem. Eng. 8 (5) (2020) 104026.
[69] M. Tafu, T. Chohji, Reaction between calcium phosphate and fluoride in phosphogypsum, J. Eur. Ceram. Soc. 26 (4–5) (2006) 767–770.
[70] C.S. Sundaram, N. Viswanathan, S. Meenakshi, Defluoridation chemistry of synthetic hydroxyapatite at nano scale: equilibrium and kinetic studies, J. Hazard Mater. 155 (1–2) (2008) 206–215.
[71] D.E. Corbridge, Phosphorus: Chemistry, Biochemistry and Technology, CRC press, 2013.